Supplementary Information for

Deep mantle earthquakes linked to CO_2 degassing at the Mid-Atlantic Ridge

Zhiteng Yu[1,2,3*], Satish C. Singh[3*], Cédric Hamelin[4], Léa Grenet[2], Marcia Maia[2], Anne Briais[2], Lorenzo Petracchini[5], Daniele Brunelli[5,6]

[1]Key Laboratory of Submarine Geosciences, Ministry of Natural Resources, Second Institute of Oceanography, Ministry of Natural Resources, 310012 Hangzhou, China
[2]Geo-Ocean UMR6538, CNRS-Ifremer-UBO-UBS; 29280 Plouzané, France
[3]Université Paris Cité, Institut de Physique du Globe de Paris, CNRS; 75005 Paris, France
[4]Independant scholar, 7 Sondre Skogveien, 5055 Bergen, Norway
[5]Cnr-Istituto di Geologia Ambientale e Geoingegneria*; Roma, Italy*
[6]Department of Chemical and Geological Sciences, University of Modena, Italy

[*]Corresponding author: Zhiteng Yu (ztyu@sio.org.cn); Satish Singh (singh@ipgp.fr)

Contents of this document

This document contains Supplementary Figures 1-13 (pages 2-14), Supplementary Tables 1–5 (pages 15-20), and a list of references given to citations made in this document (pages 21-25).

Supplementary Figures 1-13

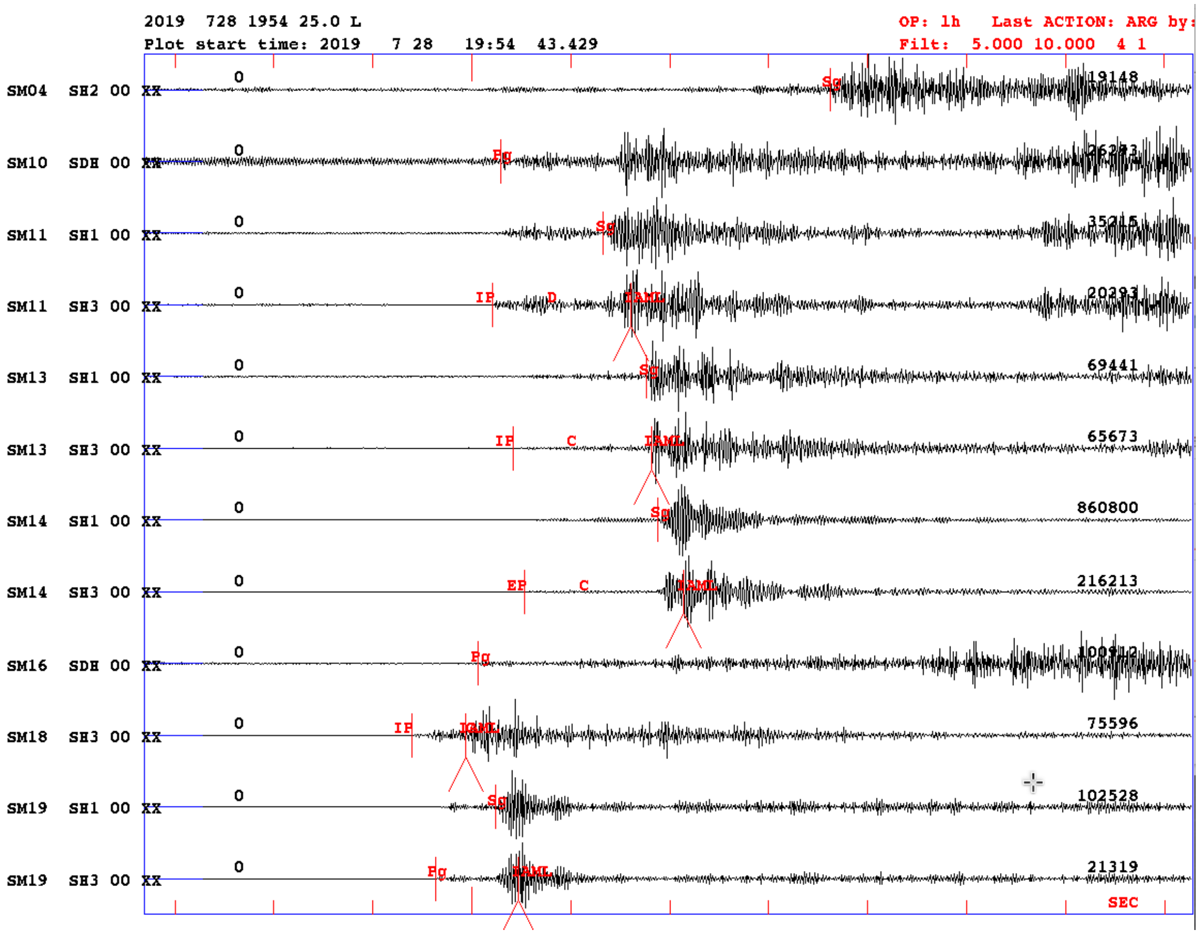

Supplementary Fig. 1. Example seismograms and picked arrivals using the SEISAN package[1]. The starting time is 2019-07-28 at 19:54. OBS stations are shown on the left for each component. SH3 indicates a vertical component, SH1 and SH2 are horizontal components, and SDH shows a hydrophone component. P-wave phases are marked by red short lines with labels of IP, Pg, and EP, and S-wave phases are marked by red short lines with a label of Sg. The amplitude used for magnitude computation is marked by a label of IAML.

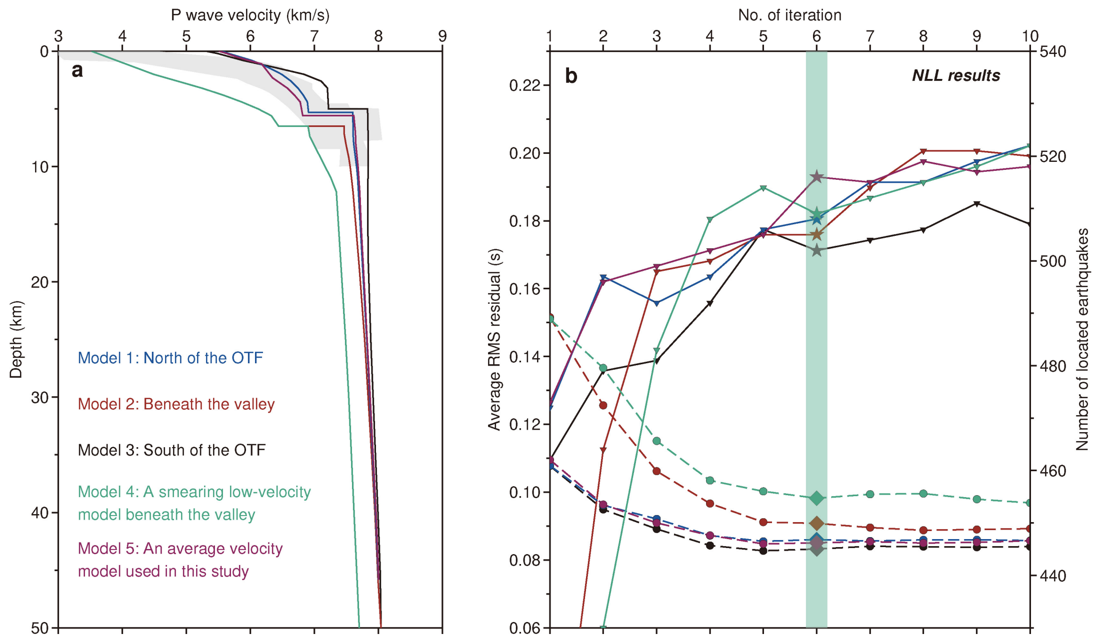

Supplementary Fig. 2. 1-D P-wave velocity models. (**a**) Five 1-D models (Models 1-5) are derived from an active-source wide-angle seismic refraction profile[2]. The smearing low-velocity model (Model 4) indicates an inverted model after the smearing test[2], in which the initial model (Model 2) is inserted by a low-velocity anomaly with a velocity reduction of 8%. Model 5 is obtained by linear interpolation of Models 1-3. The grey shade represents the velocity of the crust with an age of <7.5 Ma[3]. (**b**) Average RMS residuals (dashed lines with circles) and the number of located earthquakes (solid lines with inverted triangles) as a function of iterations using the five different 1-D models shown in (**a**). The colour represents different models shown in Fig. 2a. The vertical green bar indicates the selected results for each 1-D velocity model. Model 5 (magenta) is the selected model for the earthquake location, which has the largest number of located earthquakes, and small RMS residuals (see Methods for discussion, Supplementary Table 3).

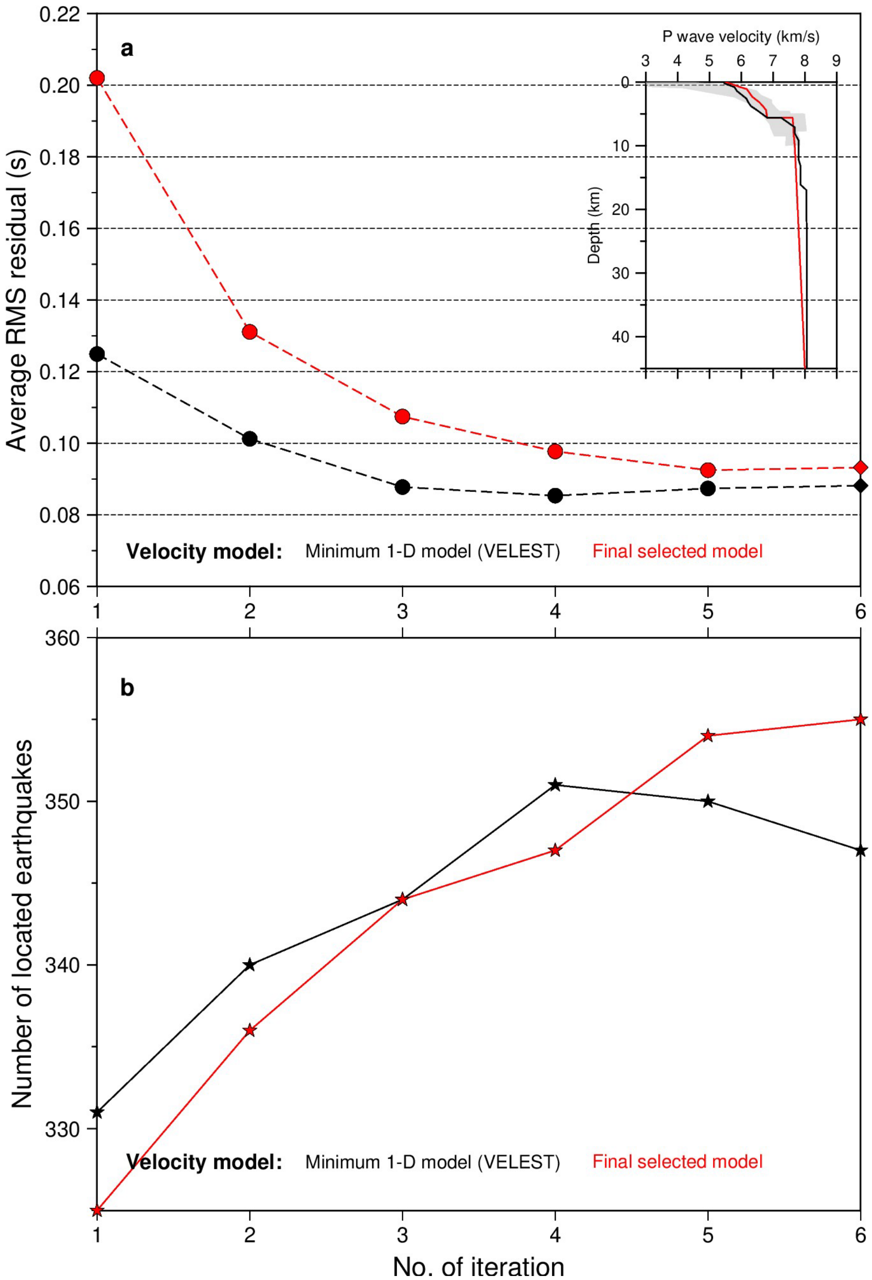

Supplementary Fig. 3. The optimum 1-D velocity model tests. (**a**) Average RMS residuals (dashed lines with circles) as a function of iteration number. A subset of 360 events with arrivals ≥6 and station GAP ≤180° is used for searching the ″minimum″ 1-D velocity model (black) by the VELEST program[4]. The selected model (Model 5 in Supplementary Fig. 2a) used for the earthquake location is shown in red circles. The insert indicates the two 1-D velocity models. (**b**) The numbers of located earthquakes as a function of the iteration number. The other labellings are the same as those in Supplementary Fig. 2.

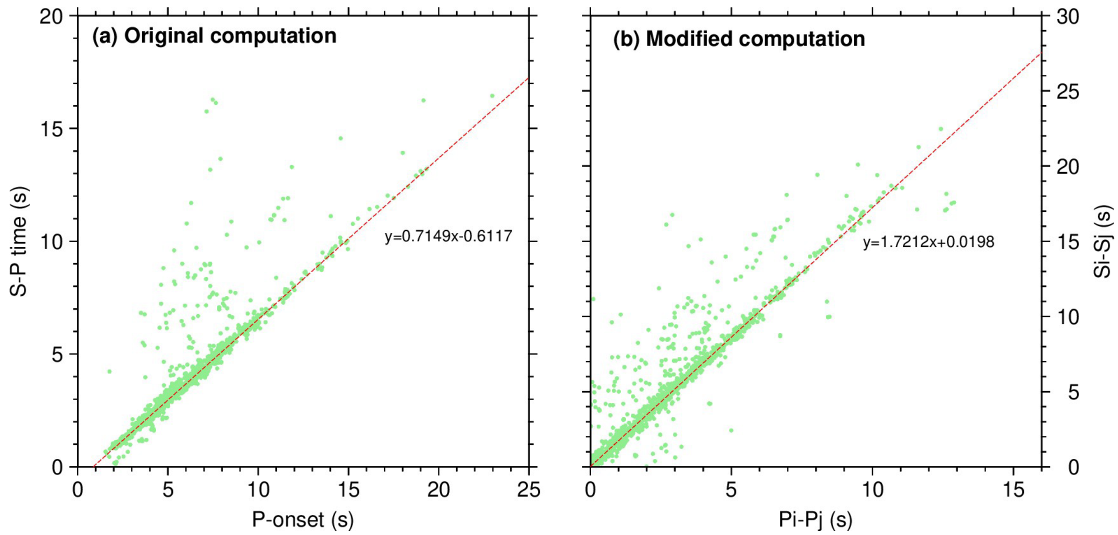

Supplementary Fig. 4. Wadati diagrams. (**a**) Green dots represent the original P-onset (P-wave onset) versus S-P time (S-wave – P-wave arrivals). (**b**) Green dots represent the modified computation showing the time differences between P-arrivals (Pi-Pj) versus those between S-arrivals (Si-Sj) for each station pair (i, j) of each event[5]. In this study, the Vp/Vs ratio is ~1.73, which is used to estimate the S-wave velocity for the earthquake location.

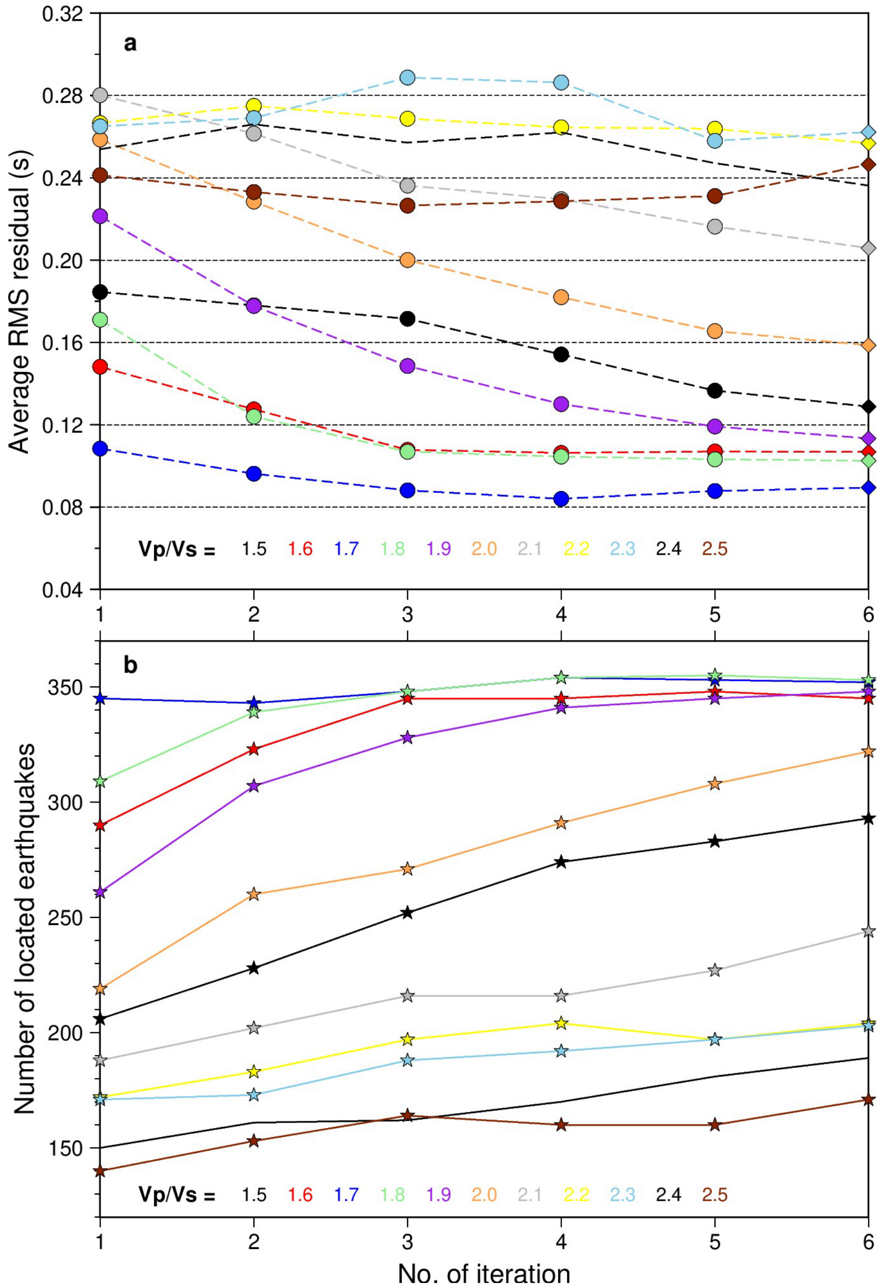

Supplementary Fig. 5. The optimum Vp/Vs ratio (or S-wave velocity model) tests. (a) Average RMS residuals (dashed lines with circles) as a function of iteration number. The colour represents different Vp/Vs ratios used in the inversion. The same subset of 360 earthquakes as in Supplementary Fig. 3 is used. (**b**) The numbers of located earthquakes as a function of the iteration number. The other labellings are the same as those in Supplementary Fig. 3.

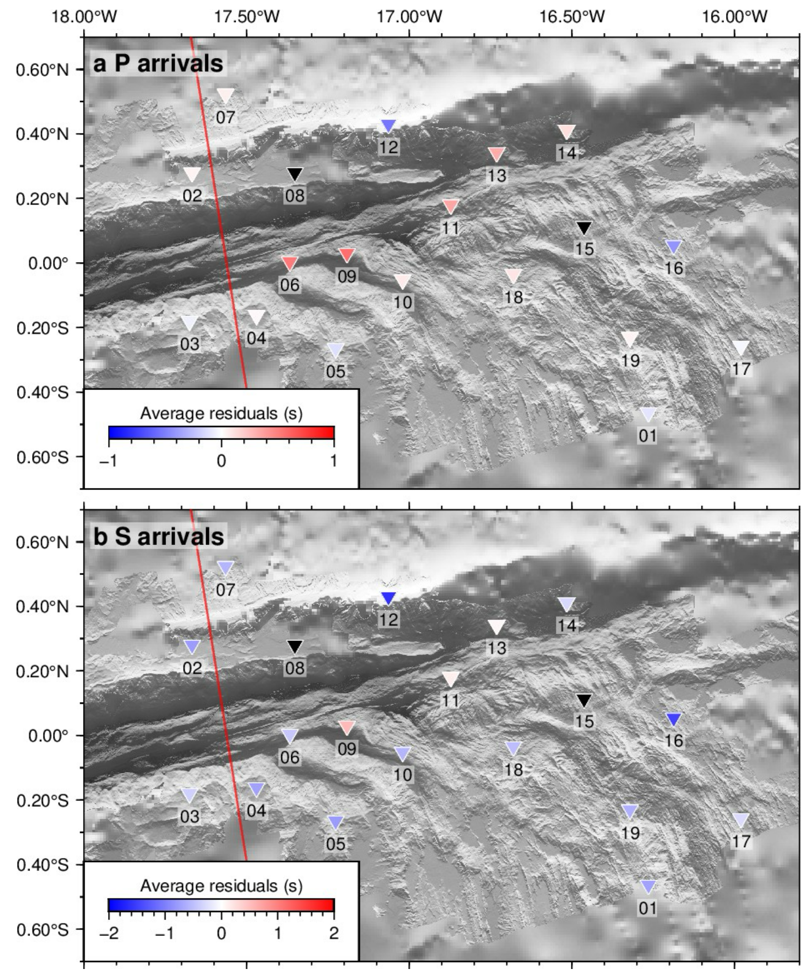

Supplementary Fig. 6. Cumulative travel time residuals. Average residuals for P- (**a**) and S-arrivals (**b**) on each station using the NonLinLoc location program[6]. The inserts show the colour scale for the average residuals. Triangles indicate the locations of ocean bottom seismometers used in this study. The red line shows the location of the seismic refraction profile[2].

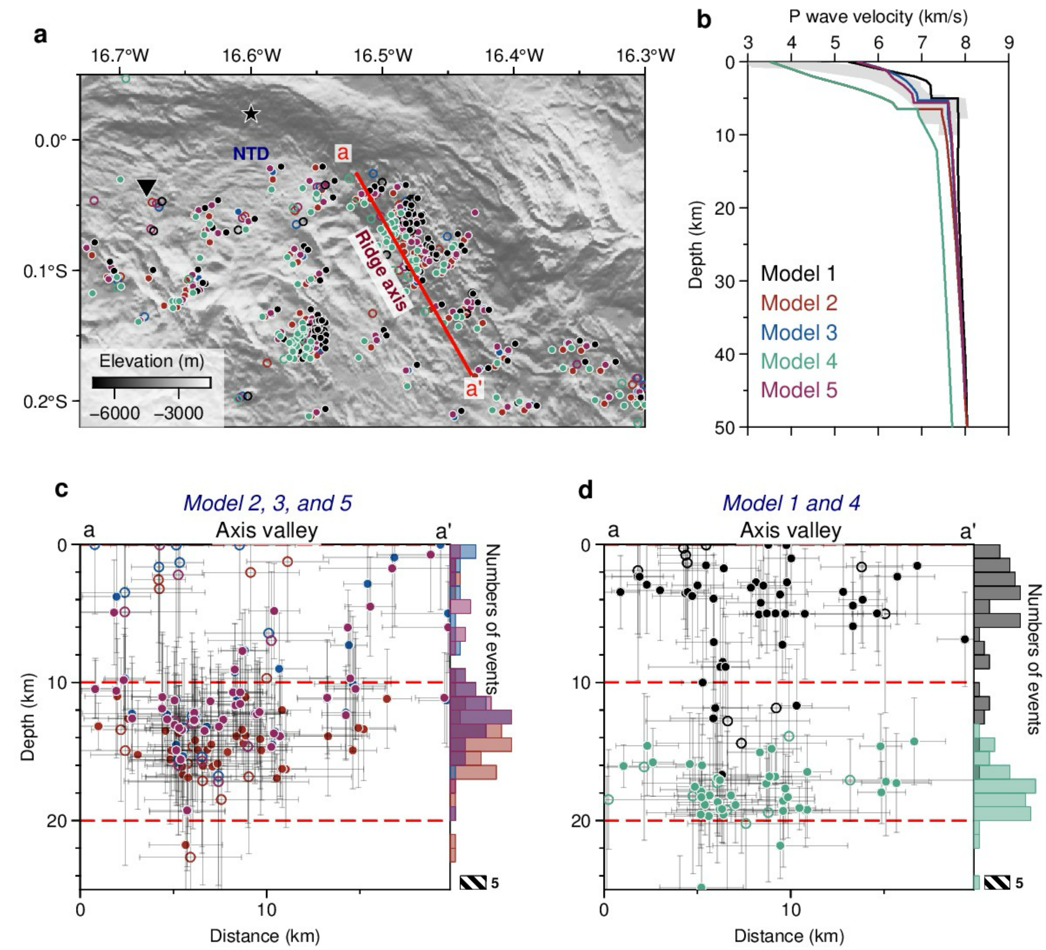

Supplementary Fig. 7. Earthquake depths along the MAR for different 1-D velocity models. (**a**) Bathymetric map and located events. Solid and open dots indicate earthquakes with a depth uncertainty of ≤5 km and 5-10 km, respectively. The colour of the circle indicates the results using the different velocity models shown in (**b**). The earthquake depths along the transect a-a′ are shown in (**c, d**). The black star indicates an inactive hydrothermal mound observed during the submersible dive[7]. (**b**) Five tested 1-D velocity models from Supplementary Fig. 2a. (**c-d**) The focal depth distribution of earthquakes along the profile (aa′) in (**a**). Grey lines mark the depth uncertainties. The histograms on the right show the depth distributions for the different 1-D velocity models in (**b**). A short column with a number is plotted for reference. See Methods for discussion.

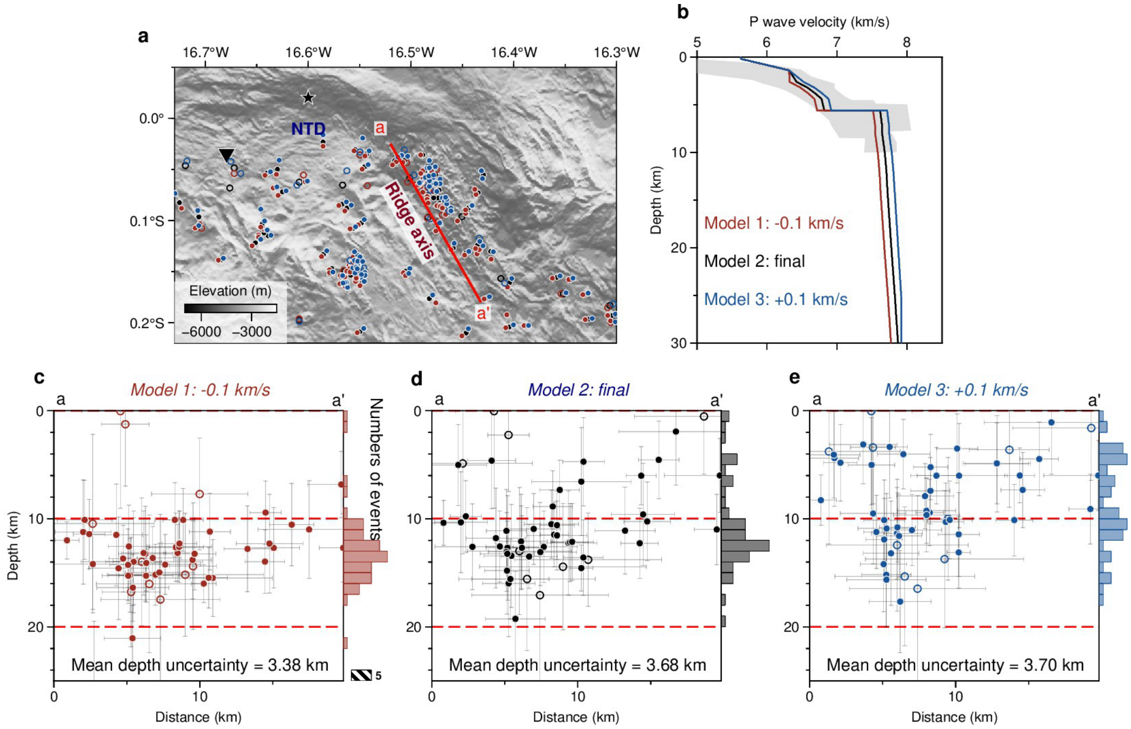

Supplementary Fig. 8. Depth resolution test along the MAR using three different 1-D velocity models. (**a**) Bathymetric map and located events. The colours represent different velocity models used for the location as shown in **b**. (**b**) Three different velocity models. Black: The final velocity used for the location. Red: The final velocity model is reduced by 0.1 km/s for all depths. Blue: The final velocity model is increased by 0.1 km/s for all depths. (**c-e**) The focal depth distribution of earthquakes along the profile (aa′) in (**a**) for the three different velocity models. The other labellings are the same as those in Supplementary Fig. 7.

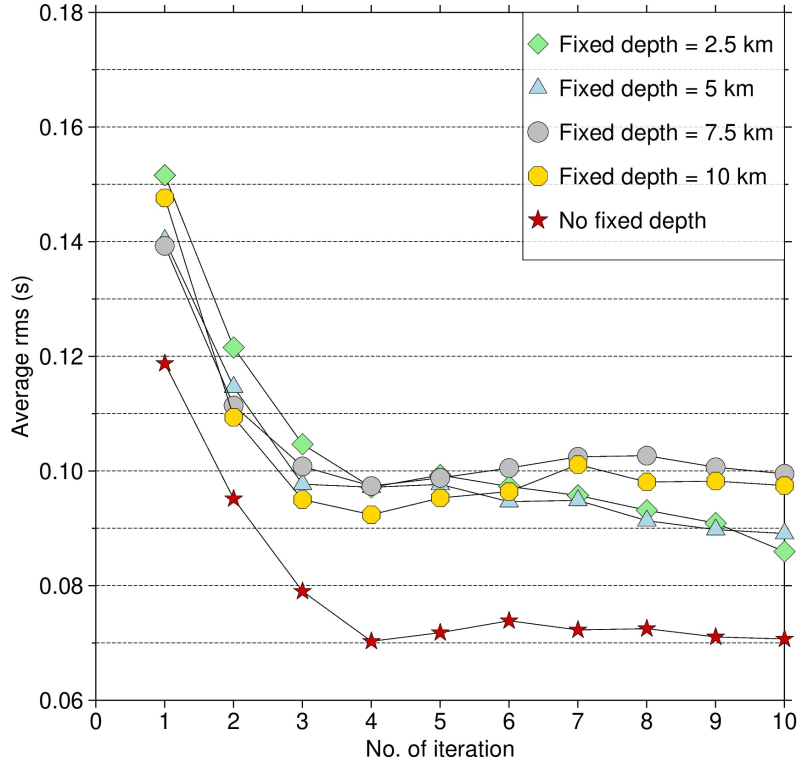

Supplementary Fig. 9. Depth-enforced resolution test. A subset of 45 events at depths between 10 and 20 km along the MAR axis is used for this synthetic test. Average RMS residuals as a function of iteration number. The coloured symbols show the misfit with focal depths fixed at shallow depths of 2.5 km, 5 km, 7.5 km, and 10 km (see the legend). The red stars indicate the RMS residuals when the depth is not fixed.

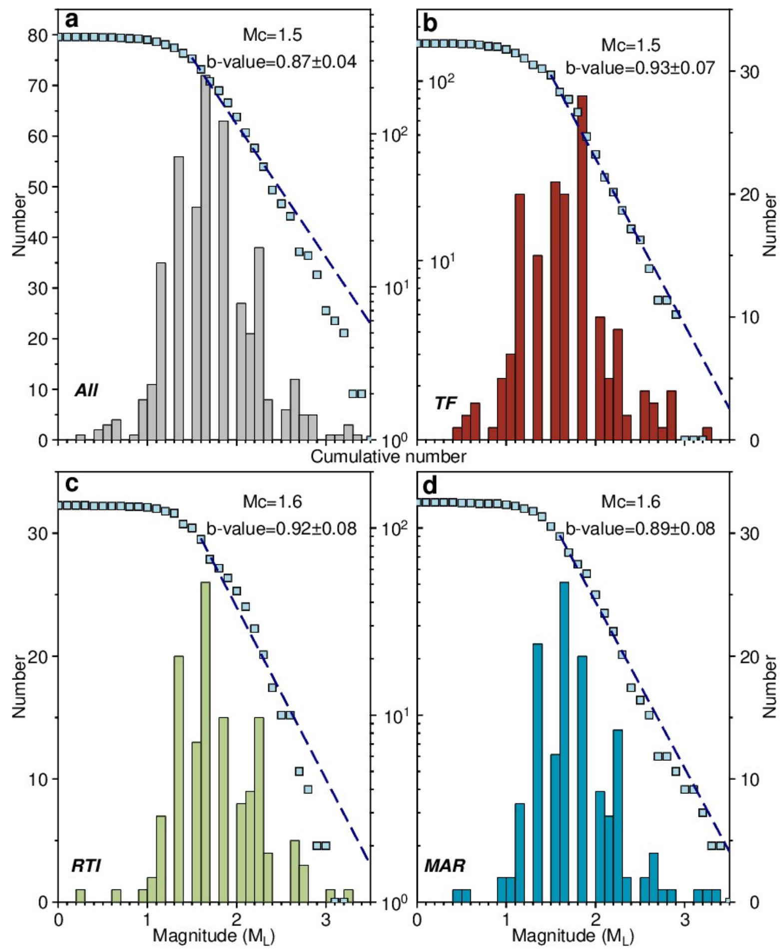

Supplementary Fig. 10. Histograms of local magnitudes (M_L). Earthquakes in the full catalogue (**a**), along the Romanche TF (**b**), in the RTI (**c**), and along the MAR (**d**) are shown in grey, red, green, and blue columns, respectively. The cumulative number of events is marked by blue squares on each map. Catalogues are analyzed using the ZMAP software[8] to obtain the magnitude completeness (M_C) and B-values.

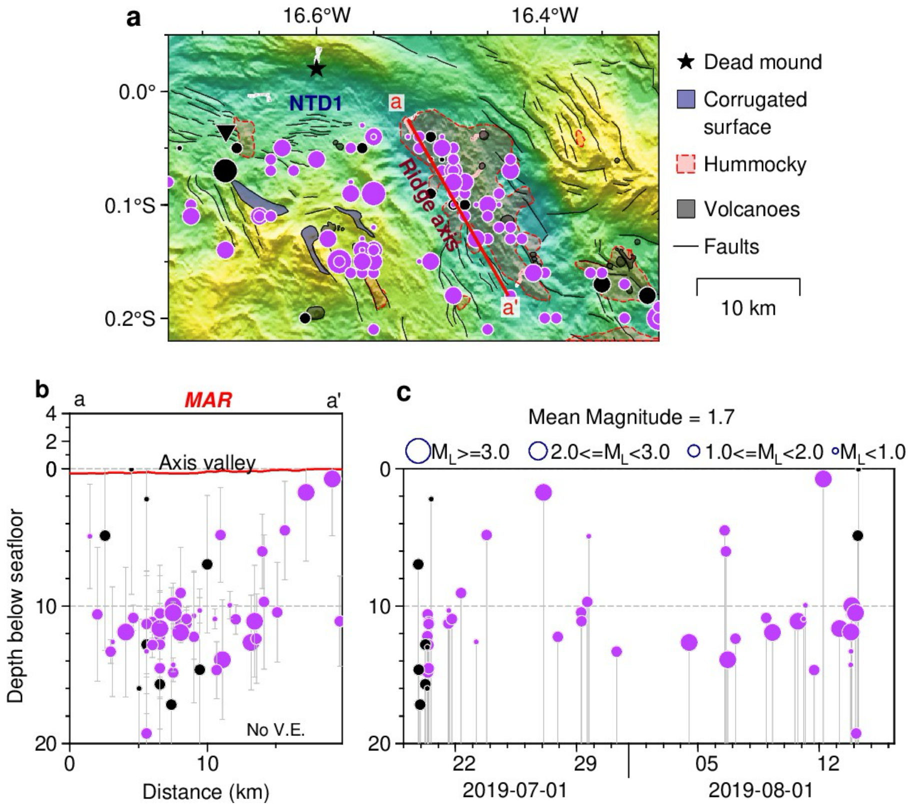

Supplementary Fig. 11. Seismicity, tectonic information, and earthquake temporal distribution along the MAR. (**a**) Bathymetric map, events, and geological information. Hummocky seafloor and volcanic cones are shown in red and grey shades, respectively. One transect along the ridge axis is shown in (**b**). Triangles mark the deployed OBSs. (**b**) The depth-section of earthquakes along profile a-a′. (**c**) The focal depth distribution of earthquakes as a function of dates from July 19 to August 16, 2019. Magnitude scales are shown at the top.

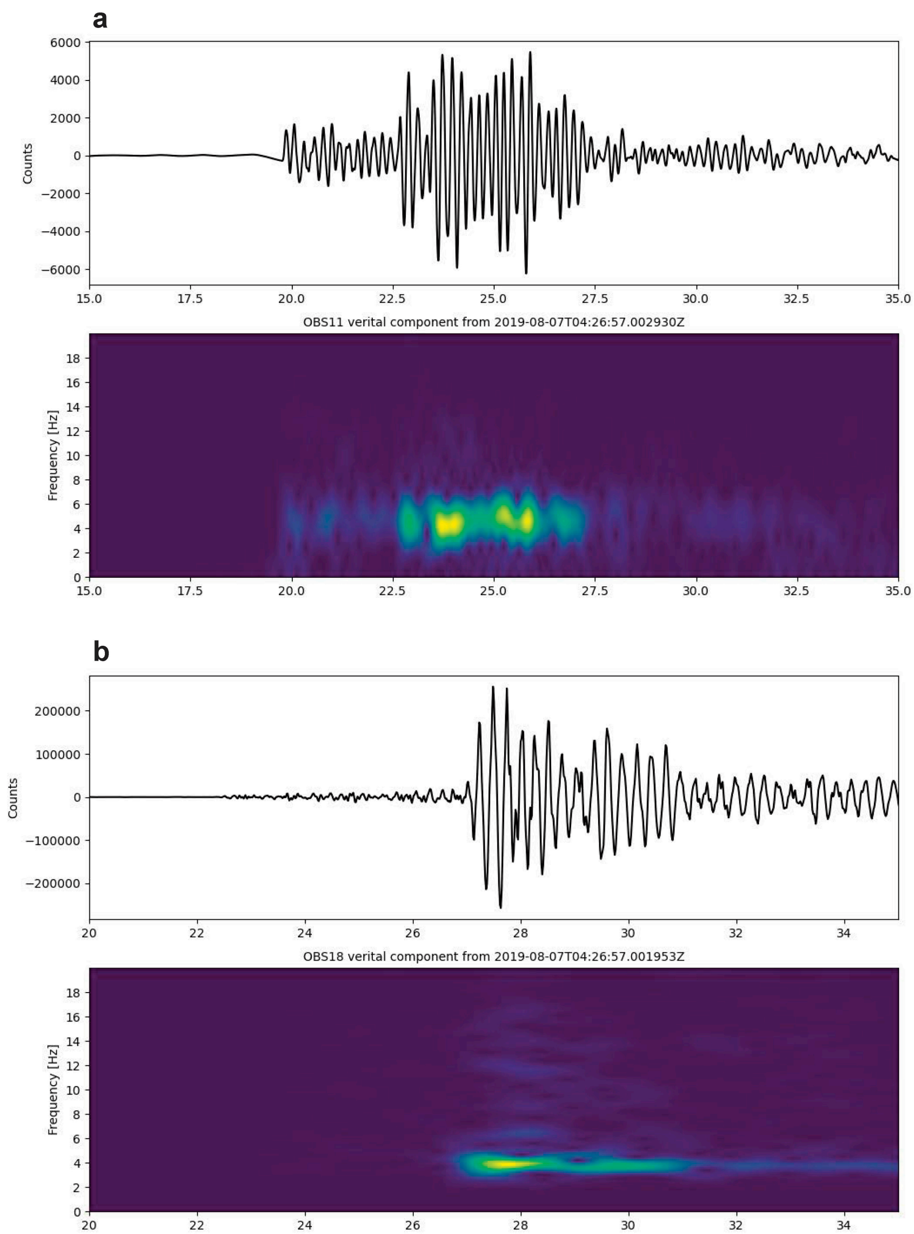

Supplementary Fig. 12. Examples of one possible long-period earthquake beneath the MAR axis. (**a**) The waveform of one example earthquake recorded at OBS11 is shown at the top, and the spectrogram plot of the vertical component is shown at the bottom. The starting time is shown in the middle, and the horizontal axis indicates the recording time in seconds. (**b**) The same earthquake was recorded at OBS18.

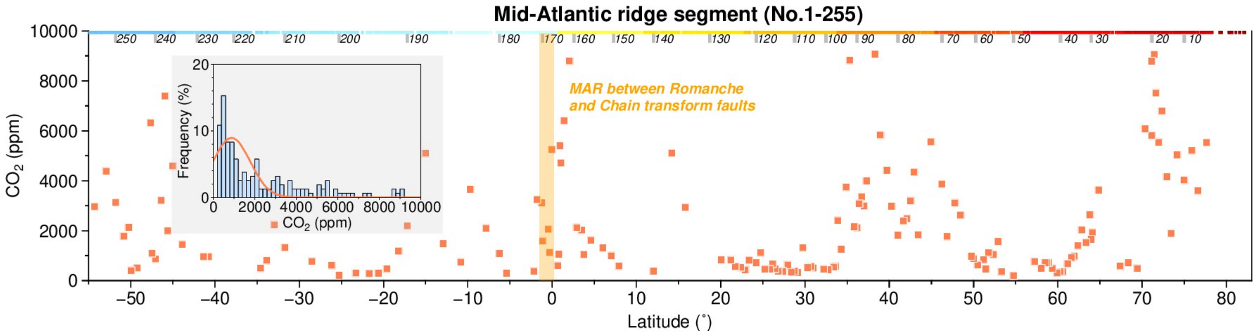

Supplementary Fig. 13. CO_2 contents in the primary magma along the whole Mid-Atlantic Ridge segments. Segment-averaged CO_2 content is extracted from Le Voyer et al. (2019)[9], and the segment number (1-255) is shown on the top. The inset histogram shows the distribution of the primary melt CO_2 contents. The orange belt shows the CO_2 contents along the MAR segments between the Romanche and Chain transform faults.

Supplementary Tables 1-5

Supplementary Table 1.

Earthquakes with location quality A-D in Figs. 2 and 3 based on well-established criteria[10–13].

Location quality	Station gap	Number of phases	One S-arrival	One arrival within a focal depth distance	One S-arrival within 1.4 focal depth distance	Uncertainty	Number of events
A	<180°	>8	Yes	Yes	Yes	<5 km	87
B	<180°	>8	Yes	Yes	No	<5 km	316
C	<180°	6-8	Yes	Yes	No	<5 km	10
D	180°-270°	>6	Yes	Yes	Yes/No	5-10 km	101

Supplementary Table 2

The maximum depth of earthquakes versus full spreading rates at 25 slow- and ultraslow-spreading Mid-Ocean Ridges. D1max and D2max indicate the maximum depth limited by several earthquakes and the deepest earthquake, respectively. Rainbow Massif (No. 22) is located in an NTD. Magmatism indicates the depths are influenced by strongly magmatic processes, e.g., hotspots and/or focused melting. Lat=Latitude; Lon=Longitude; -1=dead/inactive hydrothermal vent; RTJ=The Rodrigues Triple Junction; OCC=oceanic core complex; DF=detachment fault; TF=transform fault; MAR=Mid-Atlantic Ridge; SWIR=Southwest Indian Ridge; MCSC=Mid-Cayman Spreading Centre.

No.	**Name**	**Ridge centre**	**Area**	**Lat (°)**	**Lon (°)**	**Full rate (mm/yr)**	**Shallowest (km)**	**$D1_{max}$ (km)***	**$D2_{max}$ (km)***	**OCC/ DF**	**Vent**	**Magmatism**	**TF**
1	Amagmatic SWEAP segment [14]	SWIR	Indian	-52.37	13.30	7.8	13	20	23	Y	N	N	N
2	13°E -14°E (Oblique super-segment) [15]	SWIR	Indian	-52.38	13.50	7.8	1	16	17	N	N	N	N
3	Magmatic SWEAP segment [14]	SWIR	Indian	-52.35	13.60	7.8	10	17	20	Y	N	Y	N
4	85°E Volcanic complex [16]	Gakkel Ridge	Arctic	85.00	85.00	10.0	1	16	23	N	N	Y	N
5	Segment 1 [17]	SWIR	Indian	-25.70	69.80	12.6	0	10	10	n/a	n/a	n/a	RTJ
6	Lena Trough [18]	Fram Strait	Arctic	81.00	-5.00	12.8	N	N	14	N	N	N	N
8	Segment 8 volcano, SWRUM segment [14]	SWIR	Indian	-27.75	65.60	13.6	1	10	13	n/a	Y	Y	N
9	SWRUM segment [14]	SWIR	Indian	-27.75	65.80	13.6	1	17	20	n/a	n/a	N	N
10	Segment 27 [19]	SWIR	Indian	-37.66	50.45	14.2	3	6	8	N	-1	Y	N
11	Segment 7 [20]	SWIR	Indian	-27.58	65.95	14.2	5	12	13	n/a	n/a	N	N
12	SWIR 64°30'E [21]	SWIR	Indian	-27.85	64.50	14.5	0	14	15	Y	-1	N	N
13	Logachev Seamount [22,23]	Knipovich Ridge	Arctic	76.50	7.20	14.5	2	6	12	n/a	n/a	Y	N
14	Logachev Seamount-Amagmatic [22,23]	Knipovich Ridge	Arctic	76.20	7.20	14.5	7	16.5	20	n/a	n/a	N	N
15	Segment 28 [24]	SWIR	Indian	-37.72	49.70	14.6	2	13	15	Y	Y	N	N
16	Segment 28 [19]	SWIR	Indian	-37.72	49.70	14.6	0	16	20	Y	Y	N	N
17	Mount Dent [15]	MCSC	Caribbea	18.40	-81.75	15.0	1	7.5	9.5	Y	Y	N	Y

No.	Name	Ridge centre	Area	Lat (°)	Lon (°)	Full rate (mm/yr)	Shallowest (km)	$D1_{max}$ (km)*	$D2_{max}$ (km)*	OCC/DF	Vent	Magmatism	TF
			n										
18	Reykjanes Ridge [25]	MAR-Iceland	Atlantic	62.45	-25.80	20.0	0	7.5	12.5	n/a	n/a	Y	N
19	Lucky strike [26]	MAR	Atlantic	37.33	-32.30	20.3	1.5	3	3.3	n/a	Y	Y	N
20	Lucky strike [27]	MAR	Atlantic	37.33	-32.30	20.3	1.5	6	6.5	n/a	Y	Y	N
21	35°N-West [28]	MAR	Atlantic	35.20	-36.50	20.6	0	4	4.5	n/a	n/a	N	Y
22	Rainbow Massif [29]	MAR	Atlantic	36.20	-33.90	21.5	0	7.5	8	-1	Y	N	NTD
23	35°N-East [30]	MAR	Atlantic	35.10	-35.20	22.2	1	9	14	N	N	N	Y
24	29°N [31]	MAR	Atlantic	29.20	-43.20	22.8	2.5	7.5	8	n/a	Y	Y	N
25	23°N [32,33]	MAR	Atlantic	23.50	-45.00	23.0	0.9	8	8	n/a	n/a	N	N
26	Logatchev Massif [34]	MAR	Atlantic	14.45	-45.00	24.0	1.5	5.5	7	Y	Y	N	Y
27	26°N TAG [35]	MAR	Atlantic	26.10	44.85	24.2	0	7	8	Y	Y	N	N
28	26°N TAG [36]	MAR	Atlantic	26.10	44.85	24.2	2	7	8	Y	Y	N	N
29	13°20′N OCC [37,38]	MAR	Atlantic	13.33	-44.90	25.4	3	12	15	Y	Y	N	N
30	13°30′N OCC [37,38]	MAR	Atlantic	13.50	-44.85	25.4	4	10	12	Y	Y	N	N
31	5°S [39]	MAR	Atlantic	-5.20	-11.65	32.0	0	7	8	N	n/a	N	Y
32	0°6′S, this study	MAR	Atlantic	-0.15	-16.45	32.0	1.5	16	18.5	N	N	N	Y
33	7°12′S [34]	MAR	Atlantic	-7.20	-13.20	32.0	3	6	7	N	N	N	Y
34	7°56′S [34]	MAR	Atlantic	-7.80	-13.40	32.0	2	4	7	N	N	N	Y

Supplementary Table 3

Average location parameters for earthquakes located with the different 1-D velocity models in Supplementary Fig. 2a. For each model, an earthquake was counted when it had an RMS residual of ⩽0.3 s, a horizontal uncertainty of ⩽10 km, a vertical uncertainty of ⩽10 km, a station primary gap of <270°, and phases participated in the computation of >5. Model 5 (bold) was selected as the best-fitting 1-D velocity model, and 516 events are well located, of which two events were removed because they are out of the observation network.

Velocity model	Model 1	Model 2	Model 3	Model 4	Model 5
Number of located events	502	505	508	509	**516**
Mean RMS residual (s)	0.0832	0.0908	0.0860	0.0982	**0.0851**
Mean horizontal uncertainty (km)	2.62	2.71	2.70	2.96	**2.76**
Mean vertical uncertainty (km)	2.96	3.07	3.01	3.00	**2.93**
Mean focal depth below the seafloor (km)	9.21	13.22	11.49	15.79	**11.64**
Mean number of phases used in the computation	13.47	13.55	13.51	13.55	**13.45**
Mean station primary gap	152.24	152.62	152.82	153.29	**152.4**

Supplementary Table 4

Earthquake locations dependent on three velocity models are shown in Supplementary Fig. 8b. Only earthquakes with depth errors of ≤5 km are included in the computation of these average values.

Velocity model	Number of located earthquakes (depth error ≤10 km)	Number of located earthquakes (depth error ≤5 km)	Mean depth (km)	Mean depth error (km)	Mean horizontal error (km)	Mean RMS (s)
-0.1 km/s	511	412	12.45	1.86	2.49	0.0915
Final	516	418	11.63	1.89	2.45	0.0884
+0.1 km/s	507	407	10.10	1.84	2.43	0.0851

Supplementary Table 5

The calculated focal mechanism solutions. S1-S3 are three previous solutions for earthquake swarms from ref.[40].

No.	Longitude (°)	Latitude (°)	Depth (km)	Mechanism solution			RMS uncertainty		Number of P first motion polarities	Misfit of first motions weighted	Mechanism probability	Station distribution ratio (%)
				strike	dip	rake	fault plane	auxiliary plane				
S1	-17.1485	0.0268	11.6430	280	48	-144	30	36	13	0	63	41
S2	-17.4826	-0.0395	21.6340	121	44	-111	22	33	15	17	78	44
S3	-17.5224	-0.0468	20.8370	96	39	-153	21	33	14	13	72	46
4	-17.1022	0.0891	11.4750	257	41	-163	28	41	10	3	78	43
5	-16.8813	0.0896	6.0015	193	87	169	43	44	9	12	60	60
6	-16.8046	0.1327	6.5790	72	56	152	39	44	9	18	65	59

References

1. Havskov, J. & Ottemoller, L. SEISAN earthquake analysis software. *Seismol. Res. Lett.* **70**, 532–534 (1999).
2. Wang, Z., Singh, S. C., Prigent, C., Gregory, E. P. M. & Marjanović, M. Deep hydration and lithospheric thinning at oceanic transform plate boundaries. *Nat. Geosci.* **15**, 741–746 (2022).
3. Christeson, G. L., Goff, J. A. & Reece, R. S. Synthesis of Oceanic Crustal Structure From Two-Dimensional Seismic Profiles. *Rev. Geophys.* **57**, 504–529 (2019).
4. Kissling, E., Ellsworth, W. L., Eberhart-Phillips, D. & Kradolfer, U. Initial reference models in local earthquake tomography. *J. Geophys. Res. Solid Earth* **99**, 19635–19646 (1994).
5. Chatelain, J. L. Etude fine de la sismicité en zone de collision continentale au moyen d'un réseau de stations portables: la région Hindu-Kush Pamir. (Université scientifique et médicale de Grenoble, 1978).
6. Lomax, A., Virieux, J., Volant, P. & Berge-Thierry, C. Probabilistic earthquake location in 3D and layered models. in *Advances in seismic event location* 101–134 (Springer, 2000).
7. Maia, M. & Brunelli, D. The Eastern Romanche ridge-transform intersection (Equatorial Atlantic): slow spreading under extreme low mantle temperatures. Preliminary results of the SMARTIES cruise. in *EGU General Assembly Conference Abstracts* 10314 (2020). doi:10.5194/egusphere-egu2020-10314.
8. Wiemer, S. A Software Package to Analyze Seismicity: ZMAP. *Seismol. Res. Lett.* **72**, 373–382 (2001).
9. Le Voyer, M. *et al.* Carbon Fluxes and Primary Magma CO_2 Contents Along the Global Mid-Ocean Ridge System. *Geochem. Geophys. Geosystems* **20**, 1387–1424 (2019).

10. Hardebeck, J. & Husen, S. Earthquake location accuracy. (2010) doi:10.5078/CORSSA-55815573.
11. Gomberg, J. S., Shedlock, K. M. & Roecker, S. W. The effect of *S* -wave arrival times on the accuracy of hypocenter estimation. *Bull. Seismol. Soc. Am.* **80**, 1605–1628 (1990).
12. Chatelain, J. L., Roecker, S. W., Hatzfeld, D. & Molnar, P. Microearthquake seismicity and fault plane solutions in the Hindu Kush Region and their tectonic implications. *J. Geophys. Res. Solid Earth* **85**, 1365–1387 (1980).
13. Kissling, E. Geotomography with local earthquake data. *Rev. Geophys.* **26**, 659–698 (1988).
14. Aupart, C., Schlindwein, V., Ben-Zion, Y., Renard, F. & Jamtveit, B. *Seismic Controls on the Progress of Serpentinization at Ultra-Slow Spreading Ridges*. http://www.essoar.org/doi/10.1002/essoar.10502242.1 (2020).
15. Grevemeyer, I. *et al.* Constraining the maximum depth of brittle deformation at slow- and ultraslow-spreading ridges using microseismicity. *Geology* **47**, 1069–1073 (2019).
16. Korger, E. I. M. & Schlindwein, V. Seismicity and structure of the 85°E volcanic complex at the ultraslow spreading Gakkel Ridge from local earthquake tomography. *Geophys. J. Int.* **196**, 539–551 (2014).
17. Katsumata, K. *et al.* Microearthquake seismicity and focal mechanisms at the Rodriguez Triple Junction in the Indian Ocean using ocean bottom seismometers. *J. Geophys. Res. Solid Earth* **106**, 30689–30699 (2001).
18. Läderach, C., Schlindwein, V., Schenke, H.-W. & Jokat, W. Seismicity and active tectonic processes in the ultra-slow spreading Lena Trough, Arctic Ocean: Seismicity of Lena Trough. *Geophys. J. Int.* **184**, 1354–1370 (2011).

19. Yu, Z. *et al.* Lithospheric structure and tectonic processes constrained by microearthquake activity at the central ultraslow-spreading Southwest Indian Ridge (49.2° to 50.8°E). *J. Geophys. Res. Solid Earth* **123**, 6247–6262 (2018).

20. Meier, M. & Schlindwein, V. First In Situ Seismic Record of Spreading Events at the Ultraslow Spreading Southwest Indian Ridge. *Geophys. Res. Lett.* **45**, 10,360-10,368 (2018).

21. Chen, J., Crawford, W. C. & Cannat, M. Microseismicity and lithosphere thickness at a nearly-amagmatic oceanic detachment fault system. *Nat. Commun.* **14**, 430 (2023).

22. Schlindwein, V., Demuth, A., Geissler, W. H. & Jokat, W. Seismic gap beneath Logachev Seamount: Indicator for melt focusing at an ultraslow mid-ocean ridge? *Geophys. Res. Lett.* **40**, 1703–1707 (2013).

23. Meier, M. *et al.* Segment-Scale Seismicity of the Ultraslow Spreading Knipovich Ridge. *Geochem. Geophys. Geosystems* **22**, e2020GC009375 (2021).

24. Tao, C. *et al.* Deep high-temperature hydrothermal circulation in a detachment faulting system on the ultra-slow spreading ridge. *Nat. Commun.* **11**, 1300 (2020).

25. Mochizuki, M. *et al.* Detailed distribution of microearthquakes along the northern Reykjanes Ridge, off SW-Iceland. *Geophys. Res. Lett.* **27**, 1945–1948 (2000).

26. Crawford, W. C. *et al.* Hydrothermal seismicity beneath the summit of Lucky Strike volcano, Mid-Atlantic Ridge. *Earth Planet. Sci. Lett.* **373**, 118–128 (2013).

27. Dusunur, D. *et al.* Seismological constraints on the thermal structure along the Lucky Strike segment (Mid-Atlantic Ridge) and interaction of tectonic and magmatic processes around the magma chamber. *Mar. Geophys. Res.* **30**, 105–120 (2009).

28. Barclay, A. H. Shear wave splitting and crustal anisotropy at the Mid-Atlantic Ridge, 35°N. *J. Geophys. Res.* **108**, 2378 (2003).

29. Horning, G., Sohn, R. A., Canales, J. P. & Dunn, R. A. Local Seismicity of the Rainbow Massif on the Mid-Atlantic Ridge. *J. Geophys. Res. Solid Earth* **123**, 1615–1630 (2018).

30. Cessaro, R. K. & Hussong, D. M. Transform seismicity at the intersection of the oceanographer fracture zone and the Mid-Atlantic Ridge. *J. Geophys. Res.* **91**, 4839–4853 (1986).

31. Wolfe, C. J., Purdy, G. M., Toomey, D. R. & Solomon, S. C. Microearthquake characteristics and crustal velocity structure at 29°N on the Mid-Atlantic Ridge: The architecture of a slow spreading segment. *J. Geophys. Res. Solid Earth* **100**, 24449–24472 (1995).

32. Toomey, D. R., Solomon, S. C. & Purdy, G. M. Microearthquakes beneath Median Valley of Mid-Atlantic Ridge near 23°N: Tomography and tectonics. *J. Geophys. Res.* **93**, 9093–9112 (1988).

33. Toomey, D. R., Solomon, S. C., Purdy, G. M. & Murray, M. H. Microearthquakes beneath the Median Valley of the Mid-Atlantic Ridge near 23°N: Hypocenters and focal mechanisms. *J. Geophys. Res. Solid Earth* **90**, 5443–5458 (1985).

34. Grevemeyer, I., Reston, T. J. & Moeller, S. Microseismicity of the Mid-Atlantic Ridge at 7°S-8°15′S and at the Logatchev Massif oceanic core complex at 14°40′N-14°50′N. *Geochem. Geophys. Geosystems* **14**, 3532–3554 (2013).

35. deMartin, B. J., Sohn, R. A., Pablo Canales, J. & Humphris, S. E. Kinematics and geometry of active detachment faulting beneath the Trans-Atlantic Geotraverse (TAG) hydrothermal field on the Mid-Atlantic Ridge. *Geology* **35**, 711–714 (2007).

36. Kong, L. S. L., Solomon, S. C. & Purdy, G. M. Microearthquake Characteristics of a Mid-Ocean Ridge along-axis high. *J. Geophys. Res. Solid Earth* **97**, 1659–1685 (1992).

37. Parnell-Turner, R. *et al.* Seismicity trends and detachment fault structure at 13°N, Mid-Atlantic Ridge. *Geology* **49**, 320–324 (2021).

38. Parnell-Turner, R. *et al.* Oceanic detachment faults generate compression in extension. *Geology* **45**, 923–926 (2017).

39. Tilmann, F., Flueh, E., Planert, L., Reston, T. & Weinrebe, W. Microearthquake seismicity of the Mid-Atlantic Ridge at 5°S: A view of tectonic extension. *J. Geophys. Res. Solid Earth* **109**, B06102 (2004).

40. Yu, Z. *et al.* Semibrittle seismic deformation in high-temperature mantle mylonite shear zone along the Romanche transform fault. *Sci. Adv.* **7**, eabf3388 (2021).